Precision Medicine and Imaging

Clinical Cancer Research

Fluorescence Lifetime-Based Tumor Contrast Enhancement Using an EGFR Antibody–Labeled Near-Infrared Fluorophore

Rahul Pal[1], Homan Kang[2], Hak Soo Choi[2], and Anand T.N. Kumar[1]

Abstract

Purpose: Imaging techniques for highly specific detection of cancer cells *in vivo* can have applications ranging from preclinical drug discovery studies to clinical cancer diagnosis and surgical therapy. Although fluorescence imaging using cancer-targeted antibodies has shown promise, nonspecific probe accumulation in tissue results in significant background fluorescence, reducing detection sensitivity using traditional intensity–based continuous-wave (CW) fluorescence imaging. Here we demonstrate that fluorescence lifetime (FLT) imaging can provide significant tumor contrast enhancement over CW intensity in preclinical models of human breast cancer.

Experimental Design: Mice bearing MDA-MB-231 tumors were injected with anti-EGFR antibody conjugated to the fluorescent dye IRDye 800CW (anti-EGFR-800). Time domain fluorescence imaging was performed *in vivo* and *in situ* up to 48 hours after dye injection.

Results: Mice injected with anti-EGFR-800 showed a significantly longer FLT (0.7 ± 0.03 ns) compared with the FLT of nonspecific probe uptake in liver (0.63 ± 0.05 ns), providing a dramatic improvement in sensitivity and specificity compared with CW intensity. IgG antibody–conjugated IRDye 800CW did not show an increased FLT compared with normal tissue, suggesting that the FLT increase of anti-EGFR-800 in tumors was associated with receptor expression. Using serial surgery, we show that FLT allows the detection of smaller residual tumors in the surgical bed than possible using CW intensity.

Conclusions: Our data suggest that FLT can significantly enhance tumor contrast using fluorescently labeled antibodies, thereby accelerating the efficient clinical application of these probes for margin assessment in image-guided surgery and for highly specific detection of tumor receptors *in vivo*.

Introduction

Fluorescence imaging of solid tumors has gained significant momentum in recent years, primarily due to advances in optical imaging technologies and development of cancer-targeted fluorescent probes. Cancer cell surface marker proteins are attractive targets for cancer detection, effective drug delivery, and therapeutic interventions (1). The EGFR, a member of the ErbB family of transmembrane tyrosine kinase receptors, is a well-established key regulator of growth, invasion, and metastasis of many solid tumors including colorectal cancers (2), non–small cell lung cancer (3), triple-negative breast cancers (TNBC; ref. 4), and head and neck cancers (5). Naturally, EGFR is a suitable target for tumor detection using fluorescence imaging. EGFR-targeted fluorescence imaging can be based on either small molecule tyrosine kinase inhibitors (e.g., erlotinib, gefitinib, etc.; refs. 6, 7) or mAbs of EGFR (e.g., cetuximab, panitumumab etc. refs. 8, 9) tagged with fluorophores. In phase II/III clinical trials in combination with chemotherapy and radiotherapy, mAbs showed successful EGFR inhibition (10). In addition, mAbs induce immune response to cancer cells (4), including antibody-dependent cell-mediated cytotoxicity and T-cell–medicated immune response.

Several studies have shown the promise of fluorescence imaging of anti-EGFR antibodies conjugated to fluorescent molecules such as Alexa Fluor 488 (11), Cy5.5 (12, 13), and IRDye800CW (14, 15). Preclinical studies (16, 17) and clinical trials (14, 18) have employed antibody-based fluorescence detection of EGFR expression level (19), examination of anti-EGFR therapeutic response (16), and tumor margin assessment during surgery (14, 17). Cetuximab and panitumumab have also shown tolerable safety profiles in humans (9) after conjugation with fluorescent molecules, making them attractive candidates for targeted imaging of cancer *in vivo*.

Despite their significant promise, a major drawback with the use of antibodies for imaging is a slow clearance from the body, potentially due to their large molecular weight (20, 21). Anti-EGFR mAbs clear through the hepatobiliary system, which is usually a slow process (20). The nonspecific antibody accumulation, particularly from clearance organs such as the liver (21, 22), can result in significant background fluorescence. Previous studies primarily employed continuous-wave (CW) fluorescence imaging (23, 24), which detects the total emitted fluorescence intensity and cannot distinguish nonspecific accumulation of contrast agents (such as in liver ref. 25) from tumor-specific uptake on an absolute scale. CW intensity is also strongly dependent on imaging conditions, such as laser power, detection efficiency, and probe uptake. The strong CW intensity from nonspecific accumulation may interfere with tumor-specific signal in a clinical

---

[1] Athinoula A. Martinos Center for Biomedical Imaging, Massachusetts General Hospital and Harvard Medical School, Boston, Massachusetts. [2] Gordon Center for Medical Imaging, Massachusetts General Hospital and Harvard Medical School, Boston, Massachusetts.

Corresponding Author: Anand T.N. Kumar, Massachusetts General Hospital, Room 2301, Martinos Center, Charlestown, MA 02474. Phone: 617-726-6542; Fax: 617-726-7422; E-mail: atkumar@mgh.harvard.edu

Clin Cancer Res 2019;XX:XX–XX

doi: 10.1158/1078-0432.CCR-19-1686

Translational Relevance

Near-infrared fluorescence imaging is currently being evaluated for enhancing tumor contrast using cancer-targeted probes to enable accurate surgical resection of tumors while minimizing loss of healthy tissue. Despite enhanced tumor fluorescence intensity, fluorescence from nonspecific accumulation of targeted probes in healthy tissue reduces overall contrast, sensitivity, and specificity. In this report, we show that fluorescence lifetime detection can dramatically improve tumor sensitivity and specificity in the presence of large background fluorescence in a mouse tumor model of human breast cancer. Both the tumor model and probe used in this study have direct clinical relevance. At least two anti-EGFR antibodies, namely, panitumumab and cetuximab, have been shown to be safe for human use in IND-directed clinical trials for fluorescence-guided surgery. The work presented in this article therefore has immediate translational relevance both for intraoperative image-guided surgery and for comprehensive margin assessment in excised resection specimen postsurgery.

setting (26–28), thereby lowering sensitivity, increasing false positives, and limiting the size of tumors that can be resected.

An alternative approach to CW imaging is time domain (TD) fluorescence imaging, which allows the detection of fluorescence lifetime (FLT). FLT is a photophysical quantity that refers to the average time spent by a molecule (approximately nanoseconds) in its excited state, following laser excitation (29). Unlike CW intensity, FLT is largely unaffected by experimental conditions such as excitation power, probe concentration (30) and tissue uptake, and is often uniquely indicative of the local tissue environment (31). Our previous work has demonstrated a dramatic improvement in tumor/background contrast using FLT over CW imaging (32) of tumors labeled with indocyanine green (ICG), a nontargeted tumor contrast agent. Although ICG is FDA approved and has been applied for tumor imaging (33–35), it is not designed for tumor targeting and is therefore nonspecific to tumor-specific molecular expression. Here we demonstrate, for the first time, FLT-based contrast enhancement of EGFR overexpressing tumors in presence of high background fluorescence from tissue and nonspecific liver uptake, using an anti-EGFR antibody–labeled fluorophore. For the fluorescent reporter, we used IRDye 800CW (LI-COR Biosciences), a near-infrared (NIR) fluorescent molecule that is easily conjugated to peptides and antibodies via standard *N*-hydroxysuccinimide ester chemistry and has been previously used in clinical trials with panitumumab and cetuximab (9, 36). Although not explored in this article, the NIR emission of IRDye 800CW can enable deep-tissue imaging of tumors based on the FLT contrast reported in this work. We show tumor-specific FLT enhancement of IRDye 800CW-tagged monoclonal anti-EGFR antibody (anti-EGFR-800) and delineation of tumor from surrounding normal tissue with high sensitivity and specificity in a TNBC mouse tumor model. In addition, the tumor FLT of anti-EGFR-800 was unique across multiple animals within measurement error and provided strong tumor/background contrast in the presence of nearby organs with strong nonspecific uptake of anti-EGFR-800. Using a mock surgery, we show the advantage of FLT over CW for detecting small residual tumors in the surgical bed. We validate these *in vivo* results using *ex vivo* microscopy and pathology.

Materials and Methods

Cell culture

MDA-MB-231 cells were purchased from ATCC (Cat# HTB-26) and maintained in DMEM culture medium supplemented with 10% fetal bovine serum and 1% penicillin–streptomycin (Life Technologies). Cells were harvested at 70% to 80% confluency for tumor induction.

Antibody conjugation

Monoclonal anti-EGFR antibody (Clone 225, Cat# BE0278) and isotype control IgG1 antibody (Cat# BE0083) were purchased from Bio X Cell (West Lebanon, NH). The anti-EGFR antibody used in this study is a research-grade nontherapeutic biosimilar of the monoclonal antibody drug cetuximab. A high-molecular-weight protein labeling kit with IRDye 800CW (cat# 928-38040) was purchased from Li-COR. The antibodies anti-EGFR and IgG1 were conjugated with IRDye 800CW according to the manufacturers' protocol. Briefly, antibodies were diluted to 1 mg/mL concentration with PBS. The pH of the resulting protein solution was then raised to 8.5 by adding 1 M potassium phosphate buffer. Antibodies were mixed with IRDye 800CW (60 μg dissolved in 15-μL ultrapure water) and incubated for 2 hours at room temperature in the dark. The reaction product was purified using a Pierce Zeba desalting spin column (Cat# 89891). After purification of IRDye 800CW-conjugated anti-EGFR antibody (anti-EGFR-800) and IgG1 (IgG-800), the purification product typically contains less than 5% free dye, and the dye to protein ratio was measured using UV-Vis absorbance spectroscopy. Dye-to-protein ratio of 2.4:1 was found consistently for both anti-EGFR-800 and IgG-800.

Animal model

All animal studies were approved by the Institutional Animal Care and Use Committee in accordance with the animal welfare guidelines at the Massachusetts General Hospital. Eight (4- to 6-week-old) female nu/nu mice (anti-EGFR-800: $n = 5$; IgG-800: $n = 3$) were purchased from Charles River Laboratories Inc and were housed at the animal facility in Massachusetts General Hospital (Boston, MA). Animals were quarantined for 1 week and kept in a normal diet with 12-hour light and dark cycle. After 1 week, animals were anesthetized with 3% isoflurane and subcutaneously injected with 2×10^6 MDA-MB-231 cells in 1:1 PBS: Matrigel mixture. Tumor growth was monitored until 5- to 10-mm diameter was reached at least in one dimension.

TD imaging system

A previously published custom-built TD imaging system was used for *in vivo* and *ex vivo* animal studies (37). The small-animal imaging system consisted of a titanium sapphire laser (Mai Tai, Spectra Physics; 80 MHz repetition rate; 100-fs pulses) providing 770-nm excitation, a multimode fiber (Thorlabs) delivering light to the sample, and a gated intensified CCD (LaVision, Picostar, 500 V gain, 0.1- to 1-second integration time, 150 ps steps, 256 × 344 pixels after 4 × 4 hardware binning). A diffusing filter (Thorlabs, ED1-S50-MD) was used to expand the output of the optical fiber and delivered to the surface of the animal. The average total power across the illumination area (approximately

5-cm diameter) was 10 to 20 mW. Fluorescence was collected in reflectance mode using an 835/70-nm band-pass filter. TD fluorescence imaging was performed with a gate width of 500 ps and 150 ps steps for a total duration of approximately 6 ns per laser duty cycle of 12.5 ns. *In vivo* imaging was performed at multiple time points for 48 hours after probe injection. Animals were sacrificed after 48 hours and then imaged *in situ* by removing the skin from the top of the tumor and surrounding normal tissue (muscle and liver).

Image processing and data analysis

Algorithms for fluorescence image processing were implemented in MATLAB (MathWorks). CW data were generated from each TD dataset by adding the images over all the temporal gates. TD data from individual pixels were plotted as time gate versus log(counts) (Fig. 1) and the FLT was obtained by fitting the decay portion of TD fluorescence profiles to a single exponential function, $e^{-t/\tau(r)}$, where r denotes pixel location and $\tau(r)$ constitutes a lifetime map (e. g., Fig. 2). The white light image of whole animals was used to manually identify and create a region of interest (ROI) for the tumor and surrounding normal tissue (muscle/liver). The CW intensities and FLTs from pixels enclosed by the ROIs were used to calculate probability distributions for pixels as normal or tumor. ROC curves were obtained by varying the threshold for CW intensity and FLT and computing sensitivity and specificity. Sensitivity was calculated as the number of pixels within the tumor ROI above the threshold (CW intensity or FLT), divided by the total number of pixels within the tumor ROI. Specificity was calculated as the number of pixels within the normal ROI below the threshold divided by the total number of pixels within the normal ROI.

NIR fluorescence microscopy

NIR fluorescence microscopy was performed on a Nikon TE2000 with a QImaging color camera, Hamamatsu Orca R2 camera for fluorescence imaging, and IVison software for data collection. Tumors, liver, and muscle from animals injected with anti-EGFR-800 or IgG-800 were harvested after sacrifice (48 hours postinjection), fixed in 10% formalin, and embedded in paraffin. Ten-micron thick sections were obtained and images of slides without further staining were collected to identify localization of antibody–dye conjugates. Imaging was performed using a Xenon lamp passed through a 750/50-nm BP excitation filter and a 785-nm LP dichroic mirror, and fluorescence was collected through an 810/40-nm BP emission filter (Chroma Technologies). Exposure times were varied to obtain a similar maximum fluorescence value for each fluorescence image, and all NIR fluorescence images were normalized identically for all conditions of an experiment.

Histopathology and IHC

Tumors, muscle, and liver tissues were fixed in 10% formalin, embedded in paraffin, sectioned (10-μm thickness), and stained with hematoxylin and eosin (H&E) or processed for IHC with anti-EGFR antibody. For IHC, 10-μm thick paraffin-embedded tissue sections were dewaxed in xylene and rehydrated in decreasing concentration of alcohol. Antigen retrieval was performed with EDTA (pH 9.0) at subboiling temperature for 15 minutes. Tissue sections were incubated in 1:50 dilution of anti-EGFR antibody (Cat# 4267, Cell Signaling Tech.) overnight at 4°C. Secondary antibody was applied for 30 minutes at 37°C and slides were developed with DAKO HRP-compatible DAB (Cat# SF-4100, Vector Laboratories) and counterstained with Harris Hematoxylin. Images of H&E- and IHC-stained tissue sections were obtained using an upright Nikon Eclipse 80i microscope. A 20×, 0.75 NA air objective (Nikon) and a color camera MBF CX9000 were used to capture images.

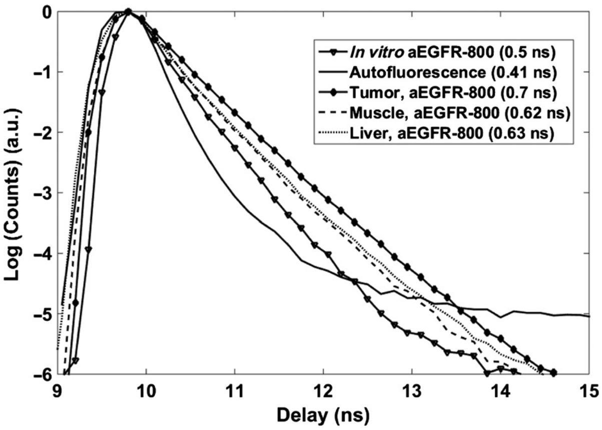

Figure 1.

TD fluorescence decay signals of tissue autofluorescence (solid line), anti-EGFR-800 (abbreviated as aEGFR-800) *in vitro* (solid line—triangles), anti-EGFR-800 *in vivo* in tumor (solid line—diamonds), muscle (dashed line), and liver (dotted line) 48 hours after injection. The decay curves are represented as the average of 3×3 pixels in TD reflectance fluorescence images. FLTs obtained from single exponential fits to the decay portion of the curves are shown in the inset.

Statistical analysis

Statistical analysis was carried out using a one-way ANOVA, followed by Bonferroni and Holm multiple comparison. *P* values less than 0.05 were considered significant: *, $P < 0.05$, and **, $P < 0.01$. The experiments were not randomized, and the investigators were not blinded to allocation during experiments and outcome assessment. Results were presented as mean ± SD.

Results and Discussion

FLT contrast between anti-EGFR-800 in tumors and normal tissue

Figure 1 shows representative TD fluorescence data for tissue autofluorescence, anti-EGFR-800 *in vitro* and *in vivo* in the tumor, and muscle and liver of a nude mouse bearing an MDA-MB-231 tumor, 48 hours after injection of anti-EGFR-800. The mean FLTs of anti-EGFR-800 *in vitro* (0.5 ns) in the tumor (0.7 ns), muscle (0.62 ns), and liver (0.63 ns) were obtained as single exponential fits to TD data as described in Materials and Methods. The autofluorescence FLT, measured before anti-EGFR-800 administration, was 0.41 ns. The FLTs in muscle and liver were therefore longer than FLT of autofluorescence, indicating that anti-EGFR-800 was retained in normal tissue 48 hours postinjection. However, the FLT of anti-EGFR-800 in tumors was longer than the FLT in muscle and liver, indicating a preferential FLT enhancement of anti-EGFR-800 in tumors.

In vivo detection of tumors in the presence of nonspecific liver uptake

In Fig. 2, we demonstrate the advantage of FLT for enhanced tumor contrast in the presence of strong nonspecific liver uptake

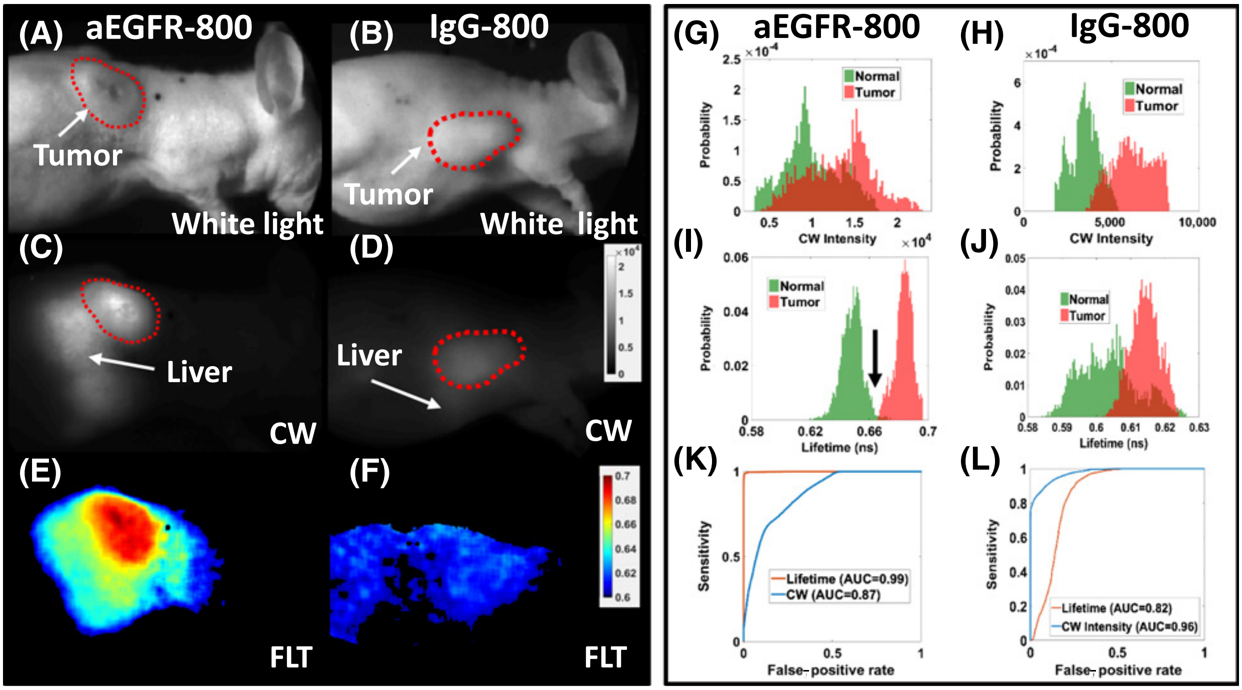

Figure 2.

In vivo TD imaging, 48 hours after intravenous administration of anti-EGFR-800 (**A**, **C**, **E**) or IgG-800 (**B**, **D**, **F**) in MDA-MB-231 tumor-bearing mice. **A** and **B,** White light images with tumor boundaries indicated by red-dotted outline. **C** and **D,** CW intensity from tumors, surrounding liver and muscle. **E** and **F,** FLT maps obtained from single exponential fits to the decay of TD data. Distributions of CW intensities (**G** and **H**) and FLT distributions (**I** and **J**) in the anti-EGFR-800– (**G** and **I**) and IgG-800– (**H** and **J**) injected animals, within tumor (red) and normal tissue (green). **K,** ROC curves calculated on the basis of CW intensity (blue) and FLT (red) thresholding for the anti-EGFR-800– (**K**) and IgG-800– (**L**) injected animals. The arrow in (**I**) represents the optimal threshold FLT for tumors used for surgical guidance study shown in Fig. 5.

in a live mouse. Shown are representative data from anti-EGFR-800– and control IgG-800–injected mice with subcutaneous tumors close to the liver. White light images (Fig. 2A and B) show the location of subcutaneous tumors outlined by red dotted lines. *In vivo* imaging of mice 48 hours post-anti-EGFR-800 injection showed that the CW intensity (Fig. 2C) in the tumor (dotted outline) and the adjacent liver (solid arrow) were comparable, making the tumor nearly indistinguishable from the liver. Animals that received IgG-800 (Fig. 2D), on the other hand, showed lower tumor fluorescence than the anti-EGFR-800 mice. Although this is expected, given IgG is a nonspecific antibody and does not bind to EGFR, it is interesting to note that the tumor was still considerably brighter than the surrounding normal muscle tissue, indicating a higher retention of IgG-800 in tumor microenvironment than in muscle. However, the relative CW intensities between the tumor and the liver in the IgG-800 group were comparable, similar to the case of the anti-EGFR-800 group.

Representative FLT maps for mice from the anti-EGFR-800 and IgG-800 groups are shown in Fig. 2E and Fig. 2F, respectively. The FLT of the anti-EGFR-800–labeled tumor was 0.7 ± 0.007 ns (mean of the pixels within the red dotted outline in Fig. 2C), which was longer than the liver FLT (0.64 ± 0.006 ns) or the surrounding muscle (0.63 ± 0.01 ns). In contrast, the tumor FLT (0.64 ± 0.005 ns) in the IgG-800 group was similar to the liver (0.63 ± 0.005 ns) and muscle (0.64 ± 0.005 ns) FLT. These observations were quantified by the histograms and ROC analysis shown in Fig. 2G–L. The histograms show the distribution of CW intensities and FLTs within (red) and outside (green) the tumor boundary as identified in the white light images. It is clear that the CW intensity distributions show considerable overlap between tumor and adjacent liver for both anti-EGFR-800– (Fig. 2G) and IgG-800– (Fig. 2H) injected animals. Tumor CW intensity for IgG-800 was appreciably lower than that for anti-EGFR-800. However, the distribution of FLTs for anti-EGFR-800 (Fig. 2I) in the normal and tumor regions showed minimal overlap, whereas IgG-800 (Fig. 2J) showed significant overlap in tumor and normal tissue FLT distributions. It is also noteworthy that the FLTs within the tumor for the anti-EGFR-800 case exhibited a narrow range with a standard error of 1.5%, suggesting that the FLT distribution within the tumor was relatively homogenous. This should be compared with the highly heterogeneous distribution of CW fluorescence intensity within and outside the tumor (Fig. 2G and H). ROC curves generated from the histograms (see Materials and Methods) show the sensitivity and specificity of tumor discrimination using CW intensity (blue) and FLT thresholding (red) of the data from the anti-EGFR-800 (Fig. 2K) and IgG-800 (Fig. 2L) animals. In the anti-EGFR-800–injected mouse, FLT (AUC = 0.99) showed a clear improvement over CW (AUC = 0.87). Notably, although tumor discrimination in the IgG-800 animal was not expected using either CW or FLT contrast, CW measurements showed strong tumor discrimination (AUC = 0.95) whereas FLT performed poorly (AUC = 0.74). Despite the better performance of IgG using CW imaging, it should be noted that the tumor CW contrast of the IgG group is not cellularly specific, as we confirm below using microscopy, and could possibly be due to enhanced permeability and retention in the tumor environment.

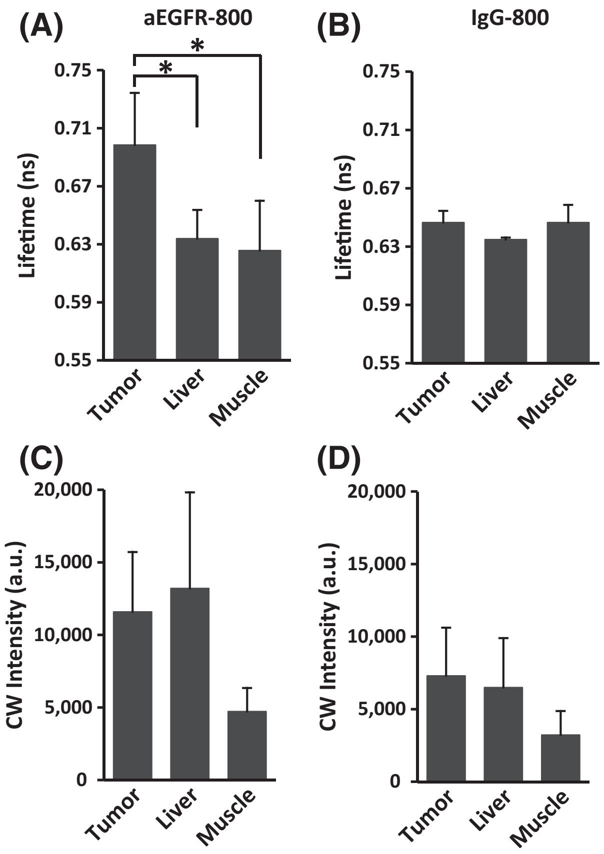

Figure 3.

In-situ quantification of FLT and CW intensity of anti-EGFR-800 or IgG-800 in tumors, liver, and muscle. FLTs for (**A**) anti-EGFR-800 and (**B**) IgG-800 in tumor, liver, and muscle; CW intensities for anti-EGFR-800 (**C**) and IgG-800 (**D**) in tumor, liver, and muscle. *, $P < 0.05$.

Furthermore, the CW contrast is dependent on probe uptake, and hence tumor size, thereby limiting the detection of small tumors as we will discuss below in the context of surgical resection.

To evaluate the statistical significance of CW and FLT contrast, we sacrificed multiple animals ($n = 4$ for anti-EGFR-800 and $n = 3$ for IgG-800) 48 hours after probe injection and quantified the *in situ* FLT and CW intensity for tumor, liver, and muscle. Figure 3A shows that the FLT of anti-EGFR-800 in tumors (0.7 ± 0.03 ns) was significantly longer ($P < 0.05$) than the FLT in liver (0.63 ± 0.02 ns) and in muscle (0.63 ± 0.03 ns). Animals that received IgG-800 (Fig. 3B) did not show a tumor-specific FLT increase, with the average FLT in tumor (0.64 ± 0.01 ns), liver (0.64 ± 0.01 ns), and muscle (0.65 ± 0.02 ns) being nearly identical across animals to within measurement error. In addition, the average liver FLT and muscle FLT were comparable between the IgG-800 and anti-EGFR-800 groups. This indicated that the FLTs observed from liver and muscle were independent of EGFR expression and were possibly due to nonspecific retention.

The CW intensity of anti-EGFR-800 (Fig. 3C) in tumor ($1.16 \times 10^4 \pm 4114.18$ a.u.) and liver ($1.32 \times 10^4 \pm 6611.63$ a.u.) was comparable as was also observed in Fig. 2C, whereas muscle showed low intensity ($0.47 \times 10^4 \pm 1614.92$ a.u.) compared with the tumor. Although the tumor/muscle CW intensity contrast was therefore high for individual animals, a large variation was observed (Fig. 3C) in the tumor and muscle CW intensities across multiple animals, possibly due to inter-animal variations in tumor size and probe uptake. Therefore, statistical comparisons based on the Bonferroni and Holm method did not show a significant difference in average CW intensities between tumor and muscle across multiple animals. For the IgG-800 group (Fig. 3F), the CW intensity was $0.67 \times 10^4 \pm 2554.38$ a.u. in tumor, $0.59 \times 10^4 \pm 2594.1$ a.u. in liver, and $0.27 \times 10^4 \pm 1440.77$ a.u. in muscle. Similar to the anti-EGFR-800 group, the CW intensity in tumor, liver, and muscle in the IgG-800 group was not significantly different when averaged over all animals.

Ex vivo validation of EGFR expression and cellular specificity of anti-EGFR-800 fluorescence from tumors

We performed fluorescence microscopy of excised tissue to confirm tumor localization of anti-EGFR-800 in tumors, liver, and muscle. Fluorescence microscopy of unstained tissue sections indicated intracellular localization of anti-EGFR-800 (Fig. 4A), which was observed as discrete speckles in the cytoplasm. Fluorescence intensity in the liver (Fig. 4B) was primarily confined in the sinusoids and central vein, indicating nonspecific accumulation of anti-EGFR-800. These microscopy data indicate that the CW intensity observed from the liver in Fig. 2C originates from nonspecific anti-EGFR-800 accumulation, whereas the CW intensity from the tumor is due to cellular uptake. Muscle tissue (Fig 4C) showed low fluorescence in the myocytes, which is consistent with the low muscle fluorescence observed in Fig. 2C. Fluorescence microscopy of tumors that received the control contrast agent IgG-800 (Fig. 4D) did not show uptake of IgG-800 in tumor cells, as expected. H&E staining of the tumor confirmed the presence of cancerous cells (Fig. 4E). Similarly, H&E staining of the liver (Fig. 4F) and the muscle (Fig. 4G) indicated histologically normal liver and muscle tissue. The EGFR expression status in tumor (Fig. 4H), liver (Fig. 4I), and muscle (Fig. 4J) was confirmed with IHC. Strong EGFR expression was observed only in tumors, corroborating the intracellular localization of anti-EGFR-800 in tumors shown in Fig. 4A. The lack of EGFR expression in liver and muscle confirms the nonspecific nature of fluorescence observed in these tissues.

The *in vivo* and *ex vivo* data presented in Figs. 2 to 4 suggest that anti-EFGR-800 is both localized in cells and shows an FLT increase, whereas IgG-800 is not cellularly localized and does not show an FLT change compared with normal tissue. These results suggest that the FLT increase of anti-EGFR-800 in tumors could be attributed to probe sequestration and degradation by the cells following EGFR binding (38). Tissue environmental factors, such as pH and microviscosity, or binding to calcium and sodium ions could ultimately play a role in altering the FLT of the sequestered probe in the tumor cells (31, 39–41). The same FLT increase could therefore also occur due to other mechanisms that lead to internalization, including binding of NIR dye–conjugated antibodies to other cancer-specific cell surface receptors.

Surgical resection of anti-EGFR-800–labeled tumors based on FLT and CW intensity contrast

As discussed above, the CW fluorescence intensity is strongly dependent on tumor size, because it depends on probe accumulation in the tumor, which increases with tumor volume. The tumors considered so far were sufficiently large to produce reasonable intensity contrast against normal muscle in single animals (although there was large variation between animals).

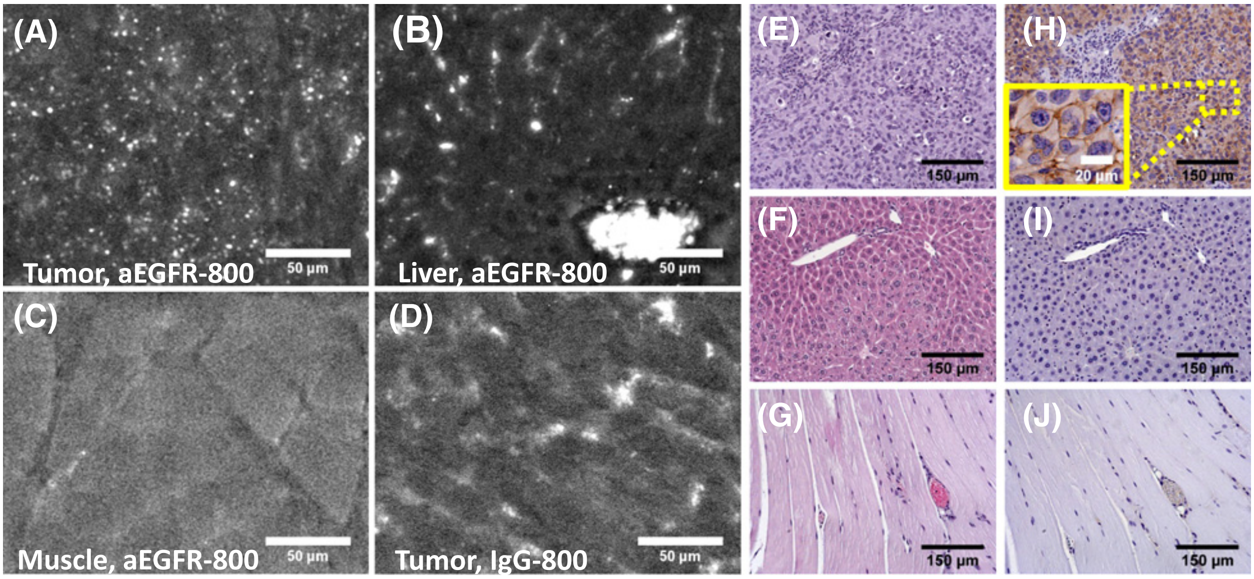

Figure 4.

Fluorescence microscopy of *ex vivo* tissue sections of a tumor (**A**), liver (**B**), and muscle (**C**) labeled with anti-EGFR-800; **D,** fluorescence microscopy of tumor from IgG-800–injected mouse; H&E staining of tumor (**E**), liver (**F**), and muscle (**G**); IHC staining of tumor (**H**), liver (**I**), and muscle (**J**). Magnification: 20×. Inset in (**H**) shows a magnified region in the tumor with predominantly membrane staining for EGFR. All *ex vivo* measurements were performed after sacrifice 48 hours after injection.

Smaller tumors will show significantly reduced tumor CW intensity due to reduced probe uptake, whereas the tumor FLT should be largely independent of tumor size, thereby enabling detection of smaller tumors in the surgical bed than possible with CW imaging. To validate this hypothesis, we performed surgical resection of an anti-EGFR-800–labeled subcutaneous MDA-MB-231 tumor. Following sacrifice, the subcutaneous tumor was exposed by removing the skin from the top of the tumor and surrounding muscle and surgery was performed in two stages (stage 1 and stage 2). A residual tumor of size of approximately 1 mm was intentionally left on the surgical bed after stage 1. Then in stage 2, the residual tumor was fully removed, exposing the underlying normal muscle. TD imaging of the whole tumor *in situ* was performed before and after the two stages of surgery. For the large initial tumor, both the CW intensity and FLT map of the whole tumor (Fig. 5A) showed strong contrast, which can be observed in the histogram distributions of intensity and FLT within the tumor (red) and surrounding normal muscle (green). CW intensity measurements showed an average tumor intensity of 12315.7 ± 1718.5 a.u. and average muscle intensity of 6607 ± 758.5 a.u. Tumor FLT was 0.7 ± 0.01 ns and muscle FLT was 0.64 ± 0.01 ns in the same ROIs used to measure CW intensity. Stage 1 surgery (Fig. 5B) showed a significantly reduced CW intensity from the residual tumor (6753.1 ± 662.1 a.u.), making it difficult to distinguish it from background fluorescence, whereas FLT in the residual tumor stayed constant within measurement uncertainty (0.69 ± 0.004 ns). Correspondingly, significant overlap of tumor and surrounding muscle is seen in histograms of CW intensity values, whereas FLT histograms did not show any significant alteration caused by the surgery and reduced tumor mass. Figure 5C shows the CW intensity and FLT map of the surgical bed following stage 2 surgery. Histograms indicate that the CW intensity range did not alter between stage 1 and stage 2. However, the FLT map of the surgical bed showed no residual long FLT component corresponding to the tumor-bound anti-EGFR-800, indicating complete removal of tumor. Confirmation of successful surgery was done by IHC staining of EGFR (Fig. 5D) in tissue sections obtained from the residual tumor (brown membranous staining pattern confirming EGFR expressing tumor cells) and the surgical bed (EGFR staining absent).

Summary

We have shown that FLTs of tumors systemically labeled with an EGFR antibody–labeled fluorescent dye, anti-EGFR-800, are significantly longer than the FLTs of nonspecific probe in muscle tissue and liver. We showed that this FLT difference can provide significant tumor contrast and sensitivity/specificity enhancement over traditional intensity-based fluorescence imaging. Although studies are under way to further understand the mechanisms behind the FLT increase in tumors compared with normal tissue, our data suggest that the FLT change of anti-EGFR-800 could be attributed to an EGFR-specific cellular uptake. Irrespective of the mechanisms underlying the observed FLT changes, our data show that the enhanced sensitivity and specificity for tumor detection using FLT can be exploited for detecting small or residual tumors that would be difficult to delineate on the basis of fluorescence intensity alone.

Several anti-EGFR antibody-tagged NIR fluorophores are currently in FDA-approved clinical trials for intraoperative imaging of various cancers (42–44). In particular, IRDye800 conjugated to panitumumab, an FDA-approved EGFR antibody, has been found to be safe for human use under multiple IND-directed clinical studies (9). Our results therefore suggest that TD imaging can serve as a new tool for cancer imaging that can provide enhanced

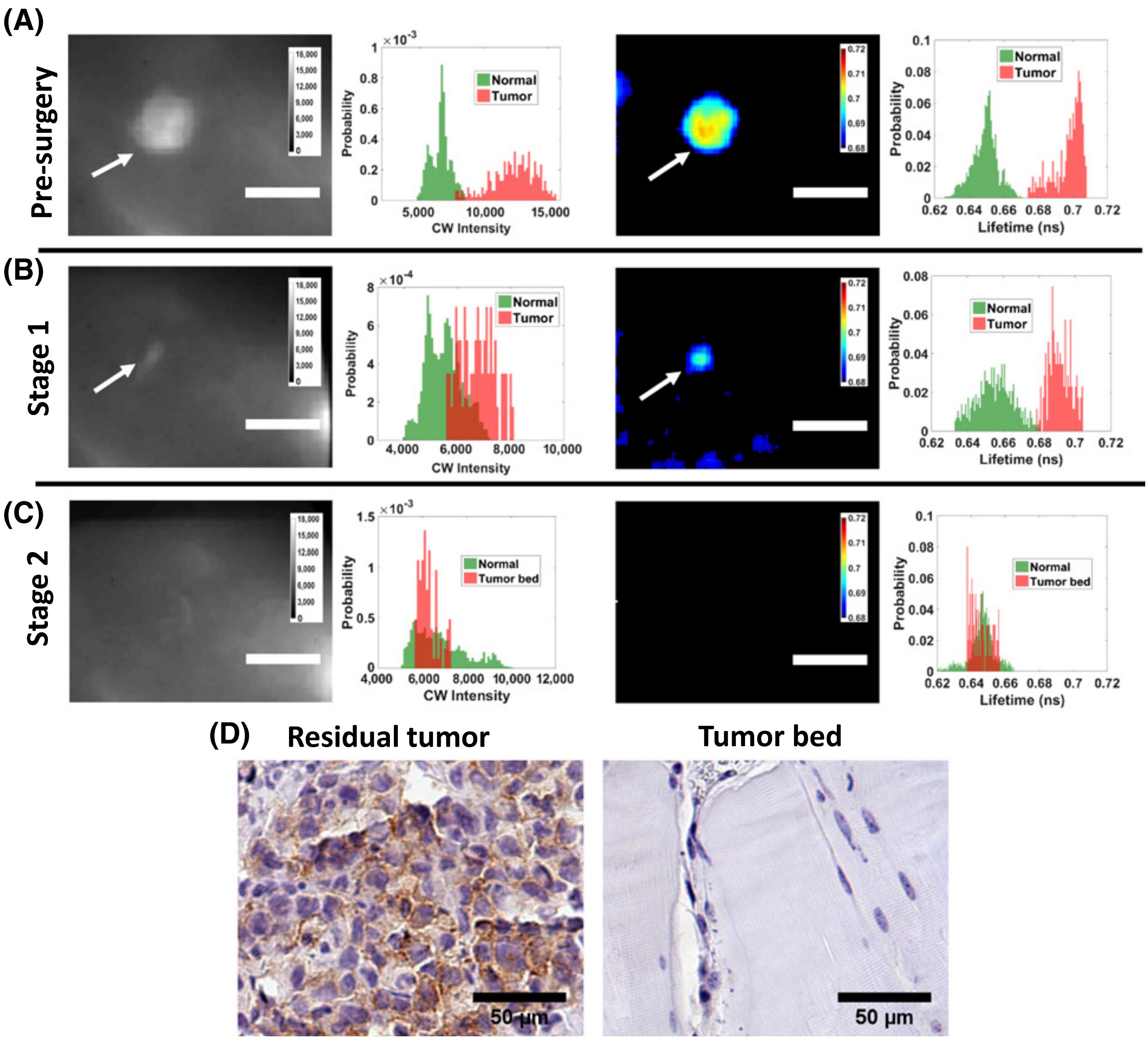

Figure 5.

In situ CW intensity and FLT maps of an MDA-MB-231 tumor before and after surgical removal of tumor mass. The animal was sacrificed 48 hours after intravenous injection of anti-EGFR-800, and TD imaging was performed after the skin was removed from the top of the tumor and surrounding muscle. CW intensity image, histogram of CW intensity, FLT map, and histogram of FLT map are shown correspondingly from left to right for the whole tumor (**A**), residual tumor (**B**), and surgical bed (**C**); (**D**) IHC for EGFR in the residual tumor obtained from (**C**; left) and surgical bed (right) is shown. Scale bar: 5-mm unless otherwise mentioned.

tumor sensitivity and specificity using panitumumab-IRDye800 and other antibody-labeled near-infrared fluorophores. Currently, FDA-approved TD imaging systems are not available for clinical use. This could be attributed to the higher cost of TD systems compared with CW but, more importantly, to the paucity of studies demonstrating the use of FLT contrast for clinical applications. We hope that our work as well as other recent preclinical studies demonstrating FLT contrast for tumor imaging using exogenous agents (41, 45, 46) will motivate the development and clinical translation of TD imaging systems in the near future. Nevertheless, an example where TD imaging of EGFR-targeted fluorescence is more immediately feasible is the comprehensive margin assessment of resection specimen from surgery. From a regulatory standpoint (47), specimen imaging studies are less cumbersome than direct intraoperative imaging, given that the imaging system will not be used directly on patients. Margin assessment of resection specimen is an important unmet need, given that pathology is slow and does not provide comprehensive assessment.

Following validation of margin assessment in resection specimen, TD imaging can be extended to intraoperative imaging of the surgical bed using exogenous agents. Existing NIR fluorescence–guided surgery systems (48) can be readily adapted to incorporate TD detection. Depending on the type of application, these systems could employ wide-field, endoscopic or handheld imaging. With successful validation of FLT imaging for clinical resection specimen and intraoperative imaging, we anticipate that TD image–guided surgery systems will become an integral part of cancer surgery. The use of NIR light can allow penetration of up to 0.5 to 1 cm in tissue using planar reflectance imaging. This should not be a limitation for surgery applications because tumors in the surgical bed are usually partially exposed or at most covered by thin layers of tissue.

Penetration depth can be enhanced up to several centimeters using NIR transmission imaging, as has been demonstrated using diffuse optical tomography of intrinsic tumor contrast in the human breast (49). FLT contrast using cancer-targeted agents can therefore be exploited with TD fluorescence tomography (37) for whole-body diagnostic imaging of deep-seated tumors in the breast. Continued efforts in developing molecular-targeted probes with distinct FLTs (41) may eventually allow multiplexed imaging for quantifying multiple tumor markers simultaneously *in vivo* (50).

Disclosure of Potential Conflicts of Interest

No potential conflicts of interest were disclosed.

Authors' Contributions

Conception and design: R. Pal, A.T.N. Kumar
Development of methodology: R. Pal, H. Kang, A.T.N. Kumar
Acquisition of data (provided animals, acquired and managed patients, provided facilities, etc.): R. Pal, H.S. Choi, A.T.N. Kumar
Analysis and interpretation of data (e.g., statistical analysis, biostatistics, computational analysis): R. Pal, H.S. Choi, A.T.N. Kumar
Writing, review, and/or revision of the manuscript: R. Pal, A.T.N. Kumar
Administrative, technical, or material support (i.e., reporting or organizing data, constructing databases): R. Pal, H. Kang, A.T.N. Kumar
Study supervision: A.T.N. Kumar

Acknowledgments

This work was supported by NIH grant R01-CA211084.

Received May 22, 2019; revised July 18, 2019; accepted August 23, 2019; published first September 3, 2019.

References

1. Divgi CR, Welt S, Kris M, Real FX, Yeh SD, Gralla R, et al. Phase I and imaging trial of indium 111-labeled anti-epidermal growth factor receptor monoclonal antibody 225 in patients with squamous cell lung carcinoma. J Natl Cancer Inst 1991;83:97–104.
2. Yarom N, Marginean C, Moyana T, Gorn-Hondermann I, Birnboim HC, Marginean H, et al. EGFR expression variance in paired colorectal cancer primary and metastatic tumors. Cancer Biol Ther 2010;10:416–21.
3. Metro G, Finocchiaro G, Toschi L, Bartolini S, Magrini E, Cancellieri A, et al. Epidermal growth factor receptor (EGFR) targeted therapies in non-small cell lung cancer (NSCLC). Rev Recent Clin Trials 2006;1:1–13.
4. Nakai K, Hung MC, Yamaguchi H. A perspective on anti-EGFR therapies targeting triple-negative breast cancer. Am J Cancer Res 2016;6:1609–23.
5. Bossi P, Resteghini C, Paielli N, Licitra L, Pilotti S, Perrone F. Prognostic and predictive value of EGFR in head and neck squamous cell carcinoma. Oncotarget 2016;7:74362–79.
6. Yang Z, Hackshaw A, Feng Q, Fu X, Zhang Y, Mao C, et al. Comparison of gefitinib, erlotinib and afatinib in non-small cell lung cancer: a meta-analysis. Int J Cancer 2017;140:2805–19.
7. Lin YT, Chen JS, Liao WY, Ho CC, Hsu CL, Yang CY, et al. Clinical outcomes and secondary epidermal growth factor receptor (EGFR) T790M mutation among first-line gefitinib, erlotinib and afatinib-treated non-small cell lung cancer patients with activating EGFR mutations. Int J Cancer 2019;144:2887–96.
8. Gao M, Su H, Lin G, Li S, Yu X, Qin A, et al. Targeted imaging of EGFR overexpressed cancer cells by brightly fluorescent nanoparticles conjugated with cetuximab. Nanoscale 2016;8:15027–32.
9. Gao RW, Teraphongphom N, de Boer E, van den Berg NS, Divi V, Kaplan MJ, et al. Safety of panitumumab-IRDye800CW and cetuximab-IRDye800CW for fluorescence-guided surgical navigation in head and neck cancers. Theranostics 2018;8:2488–95.
10. Yazdi MH, Faramarzi MA, Nikfar S, Abdollahi M. A comprehensive review of clinical trials on EGFR inhibitors such as cetuximab and panitumumab as monotherapy and in combination for treatment of metastatic colorectal cancer. Avicenna J Med Biotechnol 2015;7:134–44.
11. Mangia A, Saponaro C, Malfettone A, Bisceglie D, Bellizzi A, Asselti M, et al. Involvement of nuclear NHERF1 in colorectal cancer progression. Oncol Rep 2012;28:889–94.
12. Chen Y, Liu G, Guo L, Wang H, Fu Y, Luo Y. Enhancement of tumor uptake and therapeutic efficacy of EGFR-targeted antibody cetuximab and antibody-drug conjugates by cholesterol sequestration. Int J Cancer 2015;136:182–94.
13. Gleysteen JP, Newman JR, Chhieng D, Frost A, Zinn KR, Rosenthal EL. Fluorescent labeled anti-EGFR antibody for identification of regional and distant metastasis in a preclinical xenograft model. Head Neck 2008;30:782–9.
14. Gao RW, Teraphongphom NT, van den Berg NS, Martin BA, Oberhelman NJ, Divi V, et al. Determination of tumor margins with surgical specimen mapping using near-infrared fluorescence. Cancer Res 2018;78:5144–54.
15. van Keulen S, van den Berg NS, Nishio N, Birkeland A, Zhou Q, Lu G, et al. Rapid, non-invasive fluorescence margin assessment: optical specimen mapping in oral squamous cell carcinoma. Oral Oncol 2019;88:58–65.
16. Day KE, Beck LN, Heath CH, Huang CC, Zinn KR, Rosenthal EL. Identification of the optimal therapeutic antibody for fluorescent imaging of cutaneous squamous cell carcinoma. Cancer Biol Ther 2013;14:271–7.
17. Saccomano M, Dullin C, Alves F, Napp J. Preclinical evaluation of near-infrared (NIR) fluorescently labeled cetuximab as a potential tool for fluorescence-guided surgery. Int J Cancer 2016;139:2277–89.
18. Teraphongphom N, Kong CS, Warram JM, Rosenthal EL. Specimen mapping in head and neck cancer using fluorescence imaging. Laryngoscope Investig Otolaryngol 2017;2:447–52.
19. Bernhard W, El-Sayed A, Barreto K, Gonzalez C, Hill W, Parada AC, et al. Near infrared fluorescence imaging of EGFR expression in vivo using IRDye800CW-nimotuzumab. Oncotarget 2018;9:6213–27.
20. Mishani E, Abourbeh G, Eiblmaier M, Anderson CJ. Imaging of EGFR and EGFR tyrosine kinase overexpression in tumors by nuclear medicine modalities. Curr Pharm Des 2008;14:2983–98.
21. van Dijk LK, Hoeben BA, Kaanders JH, Franssen GM, Boerman OC, Bussink J. Imaging of epidermal growth factor receptor expression in head and neck cancer with SPECT/CT and 111In-labeled cetuximab-F(ab')2. J Nucl Med 2013;54:2118–24.
22. Sihver W, Pietzsch J, Krause M, Baumann M, Steinbach J, Pietzsch HJ. Radiolabeled cetuximab conjugates for EGFR targeted cancer diagnostics and therapy. Pharmaceuticals (Basel) 2014;7:311–38.
23. Day KE, Sweeny L, Kulbersh B, Zinn KR, Rosenthal EL. Preclinical comparison of near-infrared-labeled cetuximab and panitumumab for optical imaging of head and neck squamous cell carcinoma. Mol Imaging Biol 2013;15:722–9.
24. Cohen R, Stammes MA, de Roos IH, Stigter-van Walsum M, Visser GW, van Dongen GA. Inert coupling of IRDye800CW to monoclonal antibodies for clinical optical imaging of tumor targets. EJNMMI Res 2011;1:31.
25. Cohen R, Vugts DJ, Stigter-van Walsum M, Visser GW, van Dongen GA. Inert coupling of IRDye800CW and zirconium-89 to monoclonal antibodies for single- or dual-mode fluorescence and PET imaging. Nat Protoc 2013;8:1010–8.
26. Chen W, Shen B, Sun X. Analysis of progress and challenges of EGFR-targeted molecular imaging in cancer with a focus on affibody molecules. Mol Imaging 2019;18:1536012118823473.

27. Gong H, Kovar J, Little G, Chen H, Olive DM. In vivo imaging of xenograft tumors using an epidermal growth factor receptor-specific affibody molecule labeled with a near-infrared fluorophore. Neoplasia 2010;12: 139–49.
28. Keller DS, Ishizawa T, Cohen R, Chand M. Indocyanine green fluorescence imaging in colorectal surgery: overview, applications, and future directions. Lancet Gastroenterol Hepatol 2017;2:757–66.
29. Chen LC, Lloyd WR III, Chang CW, Sud D, Mycek MA. Fluorescence lifetime imaging microscopy for quantitative biological imaging. Methods Cell Biol 2013;114:457–88.
30. Becker W. Fluorescence lifetime imaging—techniques and applications. J Microsc 2012;247:119–36.
31. Berezin MY, Achilefu S. Fluorescence lifetime measurements and biological imaging. Chem Rev 2010;110:2641–84.
32. Kumar AT, Carp SA, Yang J, Ross A, Medarova Z, Ran C. Fluorescence lifetime-based contrast enhancement of indocyanine green-labeled tumors. J Biomed Opt 2017;22:40501.
33. Ishizawa T, Bandai Y, Ijichi M, Kaneko J, Hasegawa K, Kokudo N. Fluorescent cholangiography illuminating the biliary tree during laparoscopic cholecystectomy. Br J Surg 2010;97:1369–77.
34. Yokoyama J, Fujimaki M, Ohba S, Anzai T, Yoshii R, Ito S, et al. A feasibility study of NIR fluorescent image-guided surgery in head and neck cancer based on the assessment of optimum surgical time as revealed through dynamic imaging. Onco Targets Ther 2013;6:325–30.
35. Corlu A, Choe R, Durduran T, Rosen MA, Schweiger M, Arridge SR, et al. Three-dimensional in vivo fluorescence diffuse optical tomography of breast cancer in humans. Opt Express 2007;15:6696–716.
36. Heath CH, Deep NL, Sweeny L, Zinn KR, Rosenthal EL. Use of panitumumab-IRDye800 to image microscopic head and neck cancer in an orthotopic surgical model. Ann Surg Oncol 2012;19:3879–87.
37. Rice WL, Shcherbakova DM, Verkhusha VV, Kumar AT. In vivo tomographic imaging of deep-seated cancer using fluorescence lifetime contrast. Cancer Res 2015;75:1236–43.
38. Ceresa BP, Vanlandingham PA. Molecular mechanisms that regulate epidermal growth factor receptor inactivation. Clin Med Oncol 2008;2: 47–61.
39. Nakabayashi T, Ohta N. Sensing of intracellular environments by fluorescence lifetime imaging of exogenous fluorophores. Anal Sci 2015;31: 275–85.
40. Lakowicz JR. Principles of Fluorescence Spectroscopy. New York: Kluwer Academic/Plenum; 1999.
41. Sarder P, Maji D, Achilefu S. Molecular probes for fluorescence lifetime imaging. Bioconjug Chem 2015;26:963–74.
42. Rosenthal EL, Warram JM, de Boer E, Basilion JP, Biel MA, Bogyo M, et al. Successful translation of fluorescence navigation during oncologic surgery: a consensus report. J Nucl Med 2016;57:144–50.
43. Rosenthal EL, Warram JM, de Boer E, Chung TK, Korb ML, Brandwein-Gensler M, et al. Safety and tumor specificity of Cetuximab-IRDye800 for surgical navigation in head and neck cancer. Clin Cancer Res 2015;21: 3658–66.
44. Miller SE, Tummers WS, Teraphongphom N, van den Berg NS, Hasan A, Ertsey RD, et al. First-in-human intraoperative near-infrared fluorescence imaging of glioblastoma using cetuximab-IRDye800. J Neurooncol 2018; 139:135–43.
45. Abe K, Zhao L, Periasamy A, Intes X, Barroso M. Non-invasive in vivo imaging of near infrared-labeled transferrin in breast cancer cells and tumors using fluorescence lifetime FRET. PLoS One 2013;8:e80269.
46. Ardeshirpour Y, Chernomordik V, Hassan M, Zielinski R, Capala J, Gandjbakhche A. In vivo fluorescence lifetime imaging for monitoring the efficacy of the cancer treatment. Clin Cancer Res 2014;20: 3531–9.
47. Tummers WS, Warram JM, Tipirneni KE, Fengler J, Jacobs P, Shankar L, et al. Regulatory aspects of optical methods and exogenous targets for cancer detection. Cancer Res 2017;77:2197–206.
48. AV DS, Lin H, Henderson ER, Samkoe KS, Pogue BW. Review of fluorescence guided surgery systems: identification of key performance capabilities beyond indocyanine green imaging. J Biomed Opt 2016;21:80901.
49. Fang Q, Selb J, Carp SA, Boverman G, Miller EL, Brooks DH, et al. Combined optical and x-ray tomosynthesis breast imaging. Radiology 2011;258:89–97.
50. Raymond SB, Boas DA, Bacskai BJ, Kumar AT. Lifetime-based tomographic multiplexing. J Biomed Opt 2010;15:046011.

AACR American Association for Cancer Research

Clinical Cancer Research

Fluorescence Lifetime-Based Tumor Contrast Enhancement Using an EGFR Antibody–Labeled Near-Infrared Fluorophore

Rahul Pal, Homan Kang, Hak Soo Choi, et al.

Clin Cancer Res Published OnlineFirst September 3, 2019.